

Photonic integrated circuits with bound states in the continuum: supplementary material

ZEJIE YU,¹ XIANG XI,¹ JINGWEN MA,¹ HON KI TSANG,¹ CHANG-LING ZOU,² AND XIANKAI SUN^{1,*}

¹Department of Electronic Engineering, The Chinese University of Hong Kong, Shatin, New Territories, Hong Kong

²Key Laboratory of Quantum Information, University of Science and Technology of China, Hefei, Anhui 230026, China

*Corresponding author: xksun@cuhk.edu.hk

Published 10 October 2019

This document provides supplementary information to “Photonic integrated circuits with bound states in the continuum,” <https://doi.org/10.1364/OPTICA.6.001342>. Sections 1 and 2 describe the fabrication procedure and experimental characterization method. Section 3 provides the detailed designs and simulation results for different types of photonic devices with bound states in the continuum. Sections 4 and 5 present the theoretical analysis of the photonic potential well and the waveguide propagation loss.

1. Fabrication procedure

We fabricated the BIC devices on LiNbO₃-on-insulator wafers purchased from NANOLN, where the nominal thickness of the LiNbO₃ layer is 400 nm for the microring cavities (Figs. 3h and 3i in the main manuscript) and 300 nm for all the other devices. The fabrication process for experimental demonstration of the BICs and passive devices consists of only one step of e-beam lithography without any

etching as shown in Fig. S1a. The spinning speed for coating a 500-nm-thick layer of ZEP520A resist is 2400 r/min. For active devices like electro-optic modulators, the fabrication process shown in Fig. S1b requires an additional step of e-beam lithography and metal deposition for fabricating electrodes. The thickness of the electrodes for active devices is 80 nm.

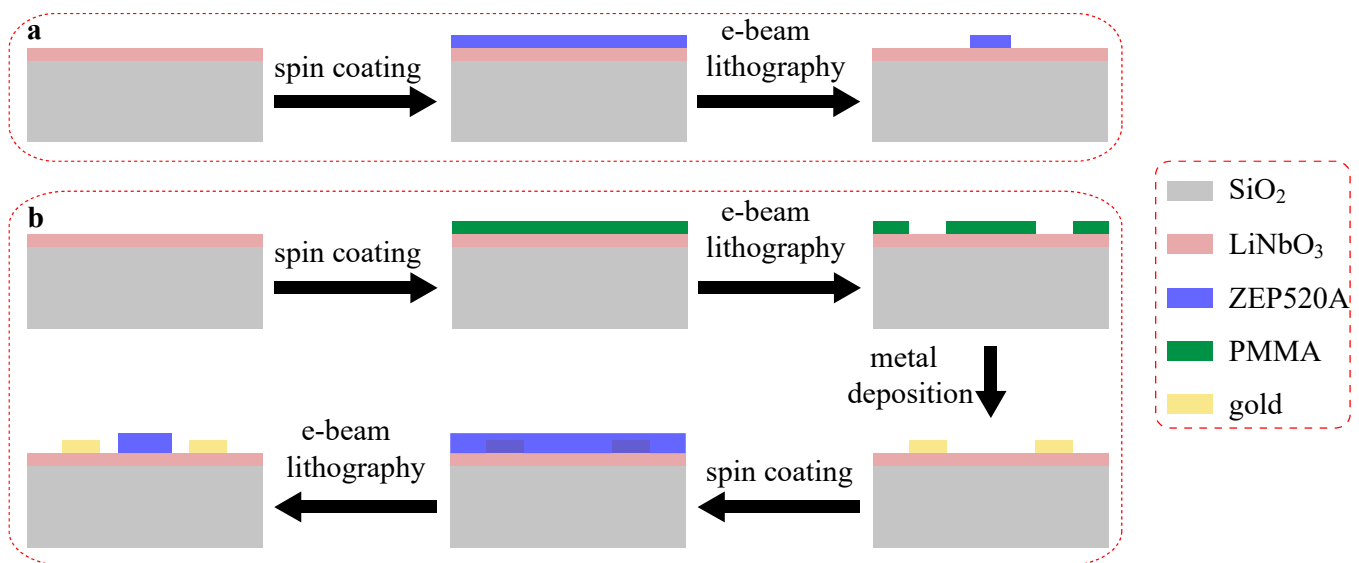


Fig. S1. (a) Procedure for fabricating the passive BIC devices. (b) Procedure for fabricating the active BIC devices.

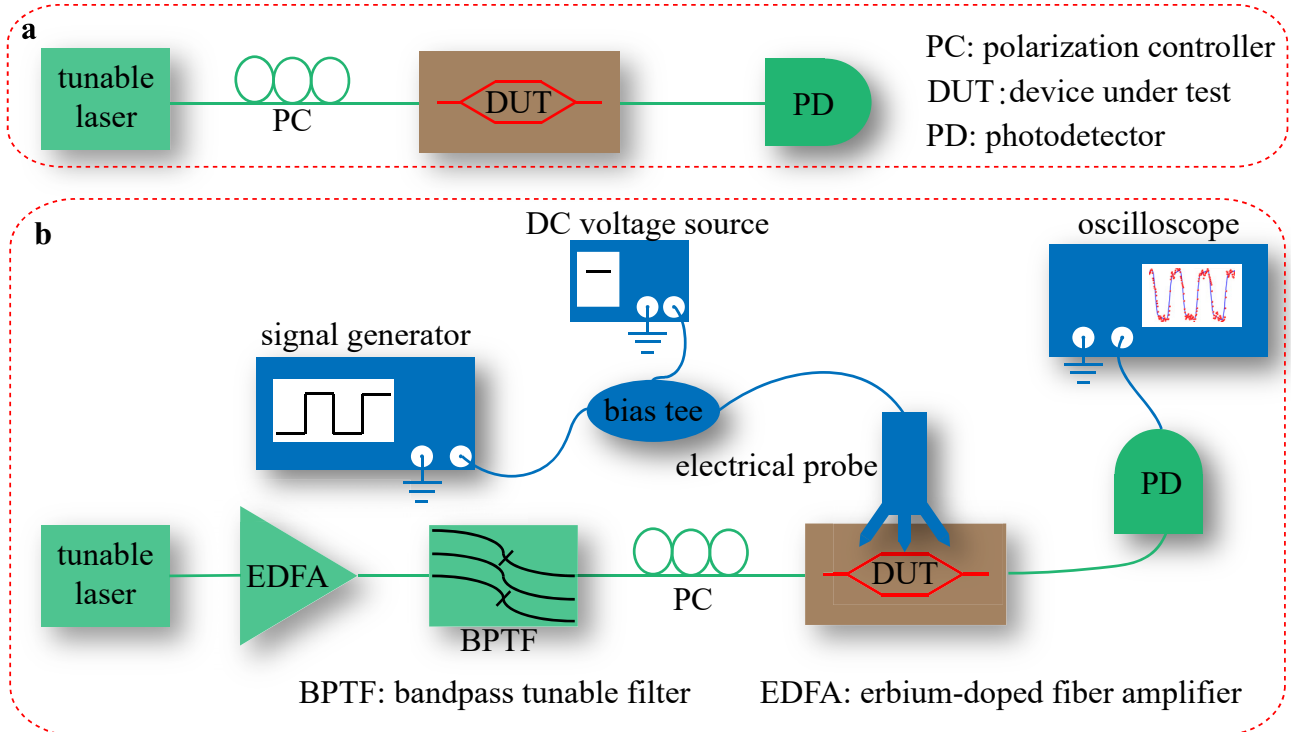


Fig. S2. (a) Experimental setup for characterizing the passive BIC devices. (b) Experimental setup for characterizing the MZI electro-optic modulators.

2. Experimental characterization

Figure S2a shows the experimental setup for characterizing all the passive BIC devices. Light from a tunable semiconductor laser is sent through a polarization controller to adjust its polarization state, then into the device under test via a grating coupler. The light coupled out of the device under test is collected by a photodetector. Figure S2b shows the experimental setup for characterizing the MZI electro-optic modulators. For the optical part, light from a tunable semiconductor laser is amplified by an EDFA, and then sent through a bandpass tunable filter to remove the background noise, followed by a polarization controller to adjust its polarization state, before reaching the device under test. The light coupled out of the device under test is collected by a high-speed photodetector. For the electrical part, a square wave added on a DC voltage is applied to the electrodes of the device under test via an electrical probe. An oscilloscope shows the waveform of the modulated light signal from the high-speed photodetector. In the experiment, the propagation loss of the straight and bent waveguides was obtained by comparing the normalized transmission of two waveguide devices on the same chip that are identical except for the waveguide lengths. We used different waveguide length difference in measurement of devices of different waveguide width. The specific value of the waveguide length difference for each type of devices was chosen based on their simulated propagation loss, because waveguides with larger (smaller) propagation loss require smaller (larger) length difference. The length difference is between 0.3 mm and 1 cm in the experiment. Last, we normalized the measured propagation loss to the same unit of dB/cm. Figures 3a and 3c in the main manuscript show the representative waveguide devices in each type. As for each waveguide structure, we conducted the device fabrication and measurement twice. The results

from the two measurements agree with each other, so for consistency purposes we chose one set of data to present in the main manuscript. The errors of the measured results are mainly attributed to the vibration of fibers, the alignment uncertainty between the grating couplers and fibers, and the fabrication uncertainty among different devices. The error of measured transmitted optical power is ~ 0.3 dB based on the measurement from five identical devices fabricated on the same chip.

3. Photonic devices with bound states in the continuum

3.1. Grating couplers

Grating couplers (Fig. S3a) are an important component for coupling light between photonic chips and optical fibers [S1]. They can be fabricated at arbitrary locations on a chip, enabling parallel characterization of a large amount of devices with large alignment tolerance. The underlying physical mechanism for grating couplers is the diffraction theory, which imposes the phase-matching condition for a free-space light beam

$$\frac{2\pi n}{\lambda} \sin \theta + \frac{2\pi}{\Lambda} = \beta, \quad (\text{S1})$$

where n is the refractive index of the upper cladding (which is air for our chip), θ is the incident angle of light, Λ is the period of the grating, and β is the propagation constant of light in the grating coupler. Equation (S1) states that the in-plane momentum of the incident light (the first term of the left-hand side) added with the momentum provided by the grating (the second term of the left-hand side) should match the momentum of light traveling in the grating (the right-hand side). The equation also indicates that the optimal wavelength λ for fiber-chip coupling depends on both the incident angle of light and the parameters of the grating.

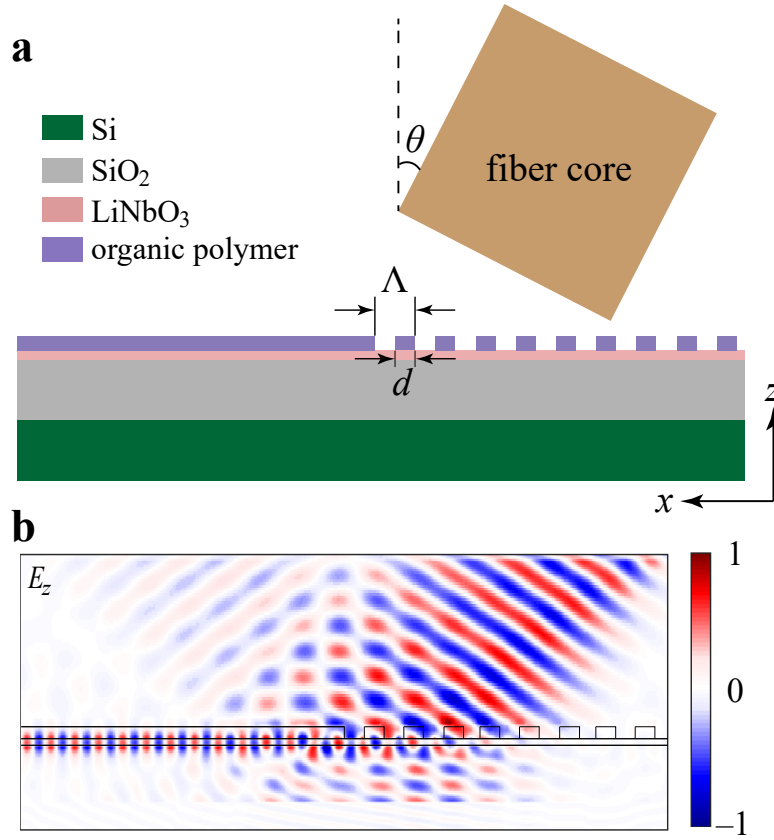


Fig. S3. (a) Illustration (side view of the cross section) of coupling between a fiber and on-chip PICs through a grating coupler. (b) Simulated electric field distribution (E_z) when light is coupled from a fiber to the on-chip PICs.

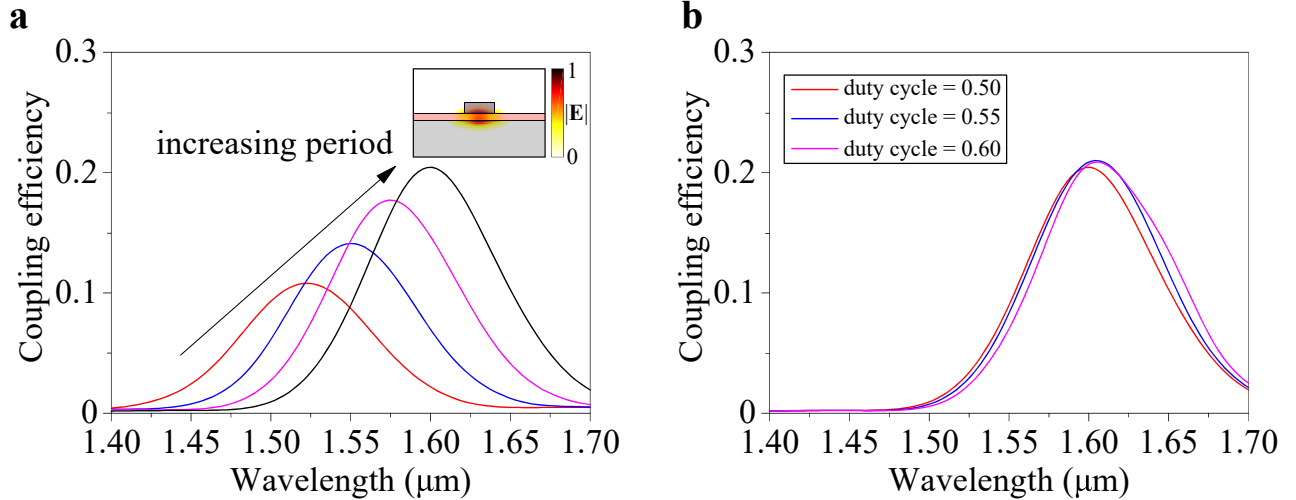


Fig. S4. (a) Simulated coupling efficiency of a grating coupler with varying grating period Λ . The inset shows the electric field ($|E|$) profile of light coupled from the fiber propagating in the PIC. (b) Simulated coupling efficiency of grating couplers with varying duty cycle d/Λ .

Figure S3b shows the numerically simulated electric field (E_z) distribution of the grating coupler by the finite-difference time-domain (FDTD) method, where the light from the fiber shines on the gratings with an incident angle of 22° . Figure S4a plots the numerically calculated coupling efficiency of a grating coupler with a varying period but fixed duty cycle d/Λ of 0.5. It shows that the optimal working wavelength of the grating coupler moves to longer wavelengths with increasing period of the grating, which agrees with Eq. (S1). The inset of Fig. S4a is the modal

profile of light in the waveguide excited by the grating coupler, which is exactly the TM mode as we desired for the BIC. Figure S4b presents the coupling efficiency of a grating coupler with a varying duty cycle but fixed period. The results indicate that the coupling efficiency is almost independent of the duty cycle. The reason is that the light traveling in the waveguide is confined mostly to the high-refractive-index LiNbO₃ slab, thus the modal properties are insensitive to the structural change of the upper low-refractive-index organic polymer.

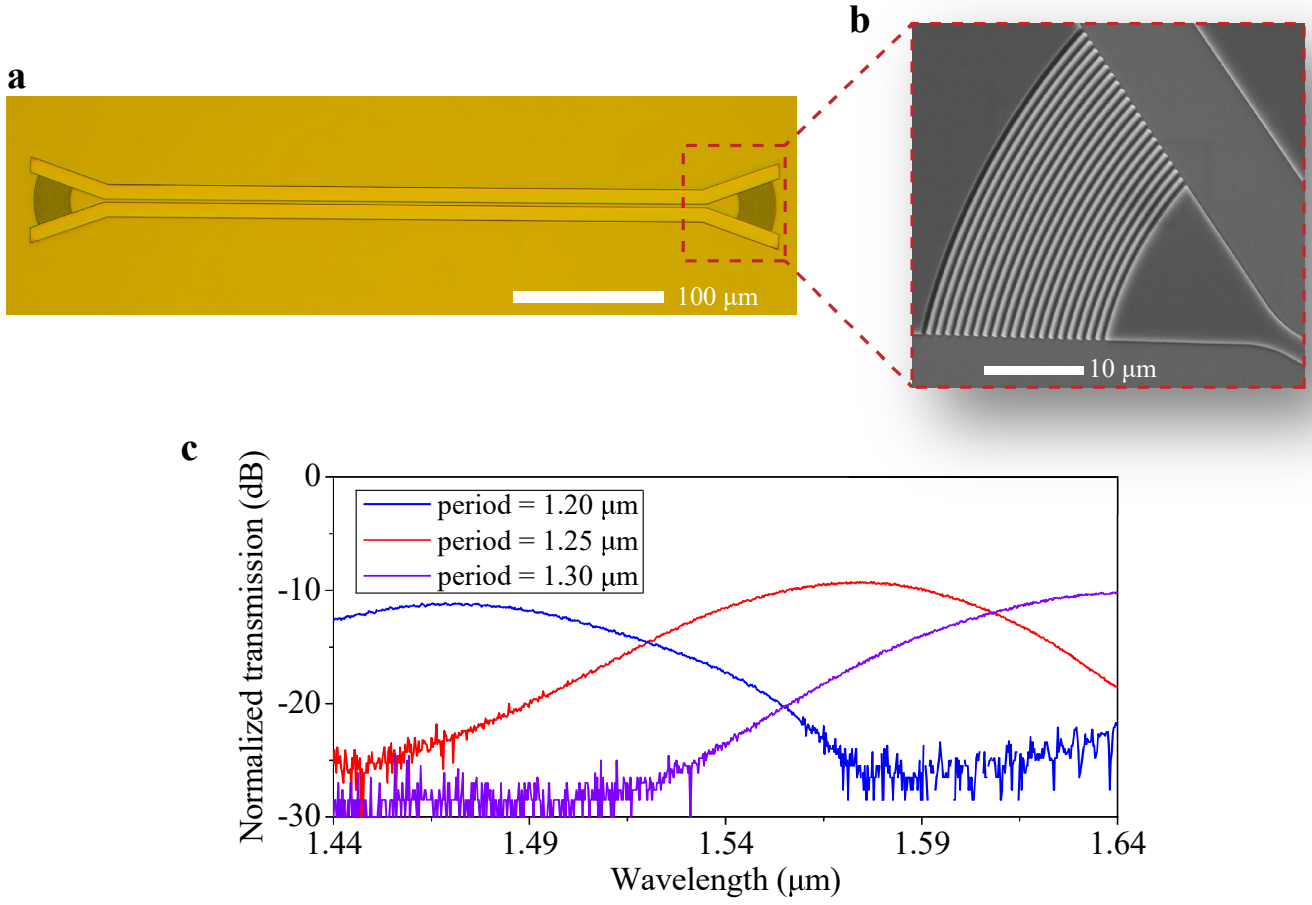


Fig. S5. (a) Optical microscope image of fabricated grating couplers connected by a straight waveguide. (b) SEM image of a grating coupler. (c) Measured coupling efficiency of a single grating coupler with different periods.

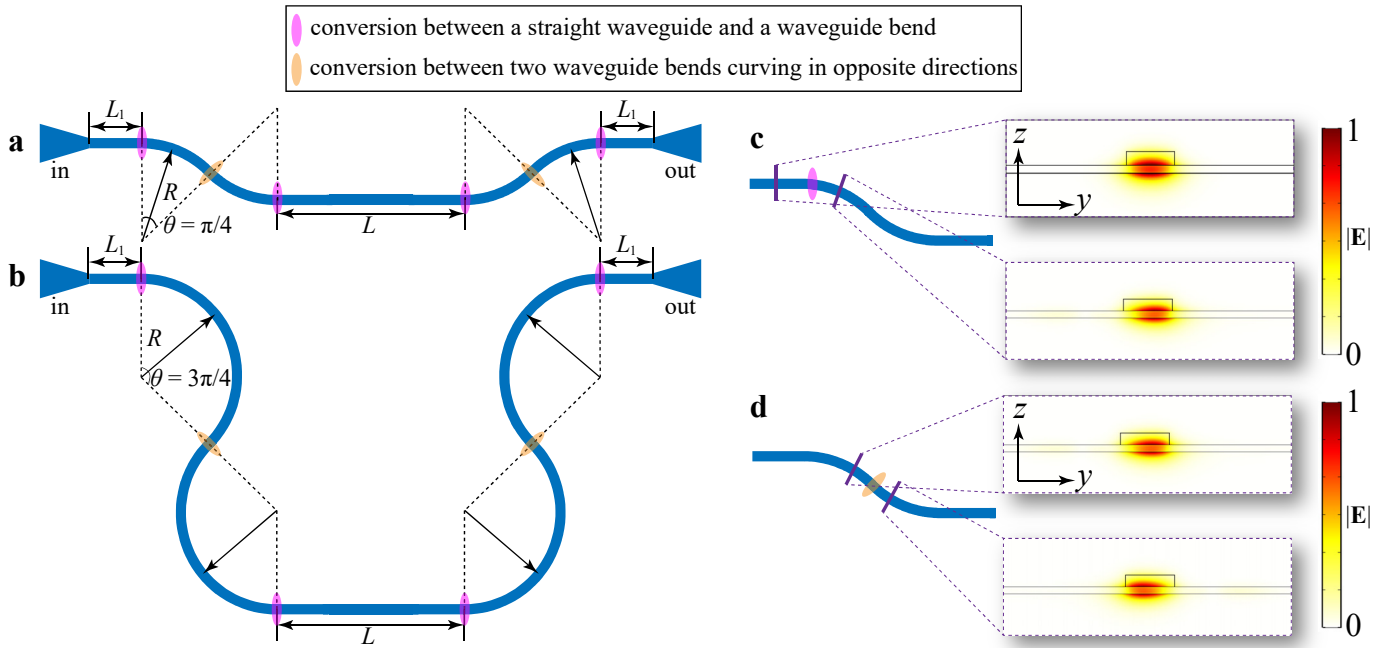


Fig. S6. (a),(b) Illustration of fabricated devices to characterize the bending loss. (c) Modal mismatch between a straight waveguide and a waveguide bend. (d) Modal mismatch between two waveguide bends curving in opposite directions.

Figure S5a shows a fabricated device with two grating couplers connected by a straight waveguide. Figure S5b is a SEM image zoomed in at the grating coupler, which has a duty cycle d/Λ of 0.5. Figure S5c plots the measured transmission spectra of a single grating coupler with

different periods. The measured minimal coupling loss of a single grating coupler is less than 10 dB, and the 3-dB bandwidth is ~ 75 nm. In addition, the operating wavelength of the grating couplers increases with their grating period, which agrees with the simulated results in Fig. S4b.

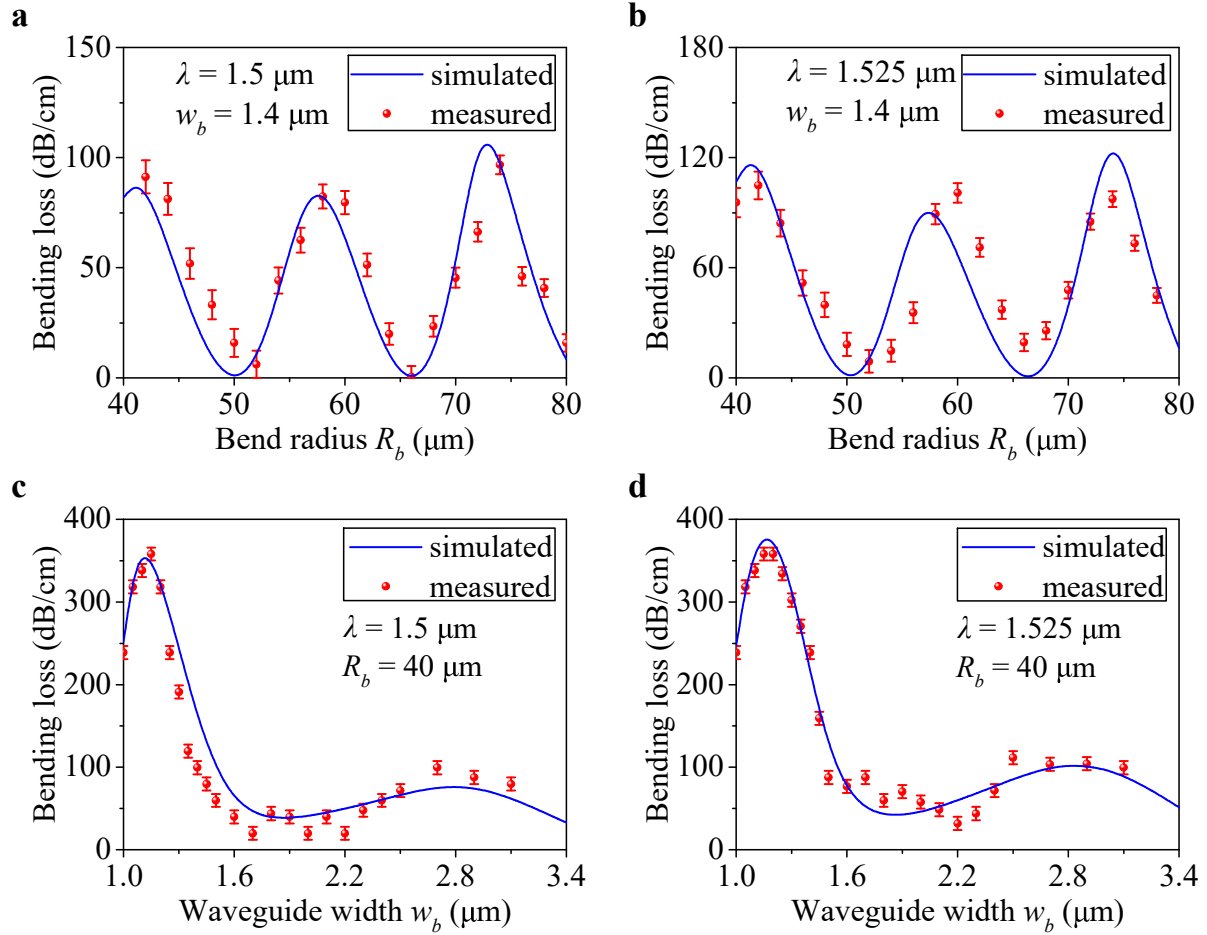


Fig. S7. (a),(b) Bending loss of waveguide bends with waveguide width of $1.4 \mu\text{m}$ and different bend radii at the wavelengths of $1.5 \mu\text{m}$ (a) and $1.525 \mu\text{m}$ (b). (c),(d) Bending loss of waveguide bends with bend radius of $40 \mu\text{m}$ and different waveguide widths at the wavelengths of $1.5 \mu\text{m}$ (c) and $1.525 \mu\text{m}$ (d).

3.2. Waveguide bends

The properties of straight waveguides can be directly measured from the structures shown in Fig. S5a, by comparing the transmission of the waveguides with different lengths. However, for bent waveguides, the characterization is slightly different. In this section, we show the details of calibrating the bending loss of waveguide bends.

Figures S6a and S6b illustrate the devices for measuring the bending loss. The total transmission loss of a device includes the insertion loss of two grating couplers, the propagation loss in the straight waveguides, the bending loss in the waveguide bends, the conversion loss at the joints of straight and bent waveguides (Fig. S6c), and the conversion loss at the joints of two waveguide bends curving in opposite directions (Fig. S6d). Comparing the two devices in Figs. S6a and S6b, the only difference is that the lengths of the respective waveguide bends are different, while the grating couplers, the straight waveguides, and the joints between different sections are exactly the same.

The bending loss was measured experimentally from devices of different parameters at different wavelengths. Figures S7a and S7b show the bending loss of waveguide bends with a fixed waveguide width $w_b = 1.4 \mu\text{m}$ but varying bend radius R_b at the wavelengths of $1.5 \mu\text{m}$ and $1.525 \mu\text{m}$, respectively. Figures S7c and S7d show the bending loss of waveguide bends with a fixed bend radius $R_b = 40 \mu\text{m}$ but varying waveguide width w_b at the wavelengths of $1.5 \mu\text{m}$

and $1.525 \mu\text{m}$, respectively. The blue lines represent the simulated results and the red dots represent the measured results. The experimental results agree well with the numerical results. It is clear that the bending loss can be minimized for certain combinations of parameters and wavelength, as predicted by the theory of BIC.

3.3. Directional couplers

Optical directional couplers are a fundamental multiport component in integrated optics and are widely employed to construct more advanced devices such as power combiner/dividers [S2], polarization rotators [S3], and mode (de)multiplexers [S4]. Figure S8a shows a fabricated directional coupler operating under the principle of BIC, where the length of the coupling region (marked by the dashed rectangle) is $95 \mu\text{m}$. Figure S8b zooms in at the coupling region, where the width of both waveguides is $1.9 \mu\text{m}$ and the gap between two the waveguides is 500 nm . Figure S8c plots the simulated normalized transmission spectra for the through and coupled ports in the wavelength range of $1.40\text{--}1.70 \mu\text{m}$. The coupling efficiency can achieve almost 100% at $\sim 1.51 \mu\text{m}$. Figure S8d plots the electric field ($|E|$) distribution of light propagating in the directional coupler, which indicates that the directional coupler operating under the principle of BIC can successfully couple light from one channel to the other as in traditional directional couplers.

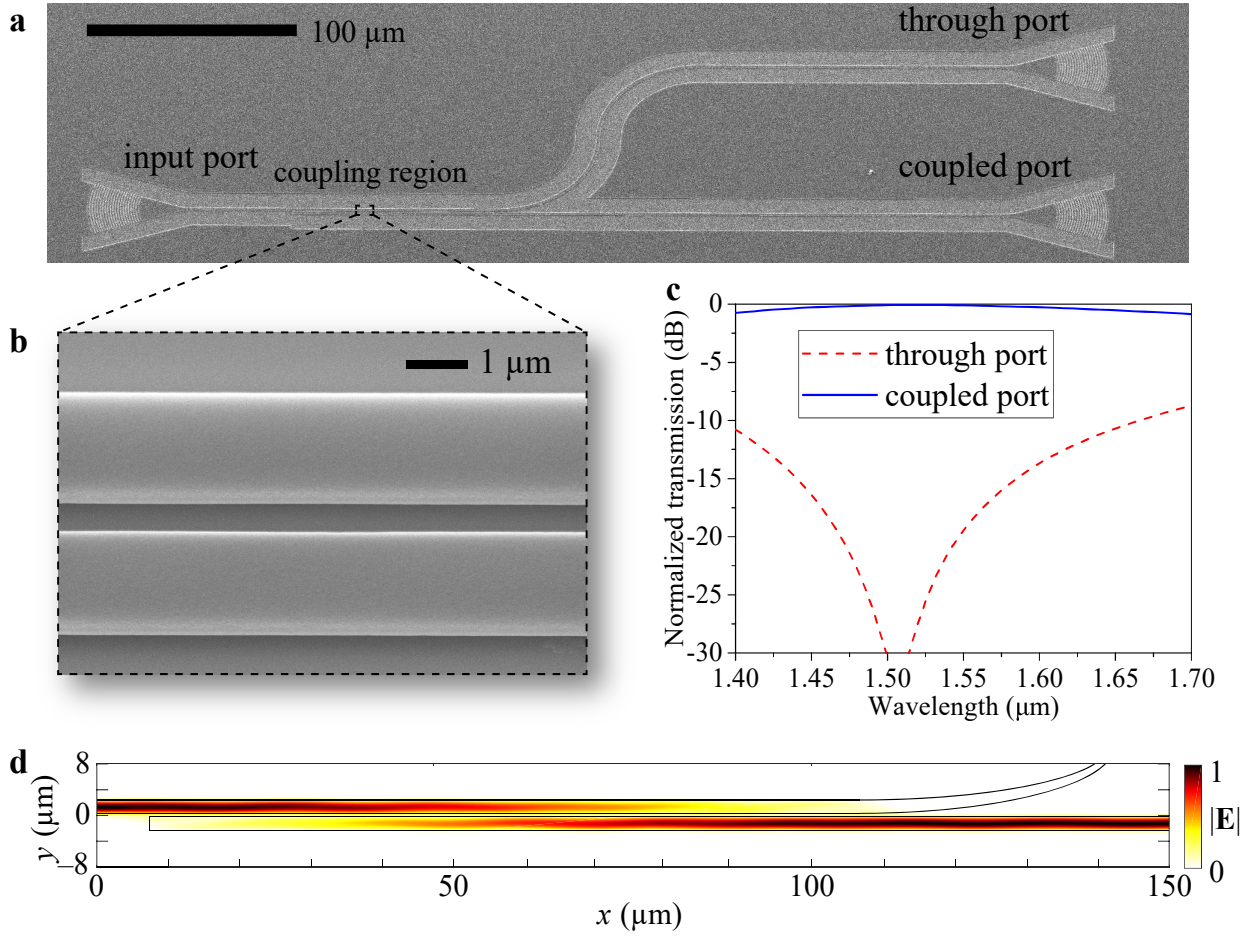


Fig. S8. (a) SEM image of a fabricated directional coupler. (b) Zoomed-in SEM image of the coupling region. (c) Simulated normalized transmission spectra for the through port (red dashed line) and the coupled port (blue solid line). (d) Electric field $|E|$ profile of light coupling from one channel to the other through the directional coupler.

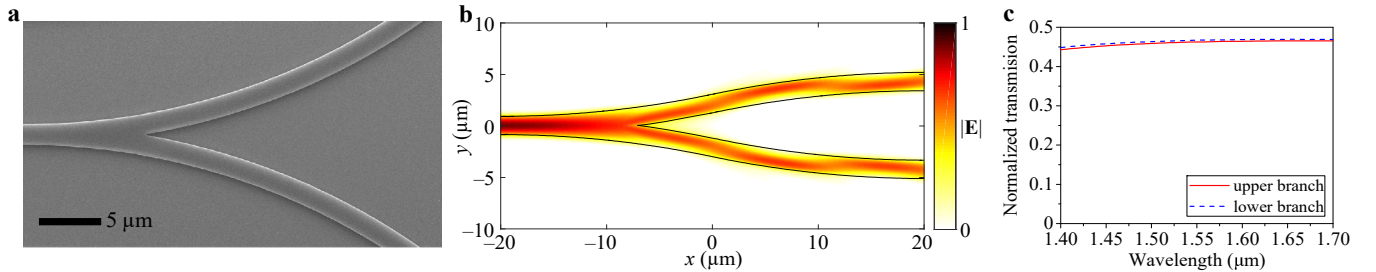


Fig. S9. (a) SEM image of a Y-branch 3-dB power splitter. (b) Electric field $|E|$ profile of light passing through the Y-branch 3-dB power splitter. (c) Simulated normalized transmission spectra of the upper (red solid line) and lower (blue dashed line) branches.

3.4. Power splitters and Mach–Zehnder interferometers

Y-branch power splitters (Fig. S9a) are used to divide light into two channels. The relation between the input and output field can be expressed as

$$E_{\text{out}}^{(i)} = \sqrt{\Gamma_i} e^{j\varphi_i} E_{\text{in}} \quad (i=1,2), \quad (\text{S2})$$

where E_{in} is the electric field amplitude in the input channel, Γ_1 and Γ_2 are the fraction of power in the two output channels, and φ_1 and φ_2 denote the phase change of the two output channels. 3-dB power splitters ($\Gamma_1 = \Gamma_2 = 1/2$) are an important optical component for optical power distribution and for construction of more advanced optical devices, such as optical switches, modulators, multiplexers, and optical phased arrays [S5–S8]. Figure S9b shows the simulated electric field $|E|$ profile of light transmitting through a 3-dB

power splitter, which indicates that light is equally divided by the Y-branch. Figure S9c plots the simulated transmission spectra for the upper and lower branches. Their transmission spectra is almost identical in the wavelength range of 1.40–1.70 μm . The deviation of their transmission away from the ideal case (i.e., 0.5) is attributed mainly to the insertion loss at the joints of straight and bent waveguides, and of two bent waveguides curving in opposite directions.

For the fabricated MZI shown in Fig. 4c in the main manuscript, its normalized transmission can be expressed as

$$T = \alpha_1 \Gamma_1 + \alpha_2 \Gamma_2 + \sqrt{\Gamma_1 \Gamma_2} \alpha_1 \alpha_2 \cos(\Delta\varphi(\lambda)), \quad (\text{S3})$$

where α_1 and α_2 are related to the propagation loss in the upper and lower arms, respectively, and $\Delta\varphi(\lambda)$ is the phase difference between the two arms. We have chosen the

waveguide parameters to satisfy the BIC condition where the propagation loss can be ignored ($\alpha_1 = \alpha_2 = 1$). Therefore, the extinction ratio can be expressed as

$$ER = \left| \frac{\sqrt{\Gamma_1} + \sqrt{\Gamma_2}}{\sqrt{\Gamma_1} - \sqrt{\Gamma_2}} \right|, \quad (\text{S4})$$

which reaches maximum if $\Gamma_1 = \Gamma_2$. The large extinction ratio shown in Fig. 4d in the main manuscript indicates that the power splitters in the MZI split light equally into the two arms.

3.5. Microcavities

It is well known that the optical losses of microcavities are usually attributed to: (i) material absorption, (ii) fabrication imperfection, and (iii) radiation to the free space for cavities of small sizes. Here, we investigate the dependence of the intrinsic quality (Q) factors of microring cavities on their radius. Figure S10a is an optical microscope image of a fabricated microring cavity, and Fig. S10b shows the intrinsic Q factors of microring cavities with different radii. Under the principle of BIC, the bending loss of a bent waveguide depends on the bend radius, so does the intrinsic Q factor of the constructed microring cavity.

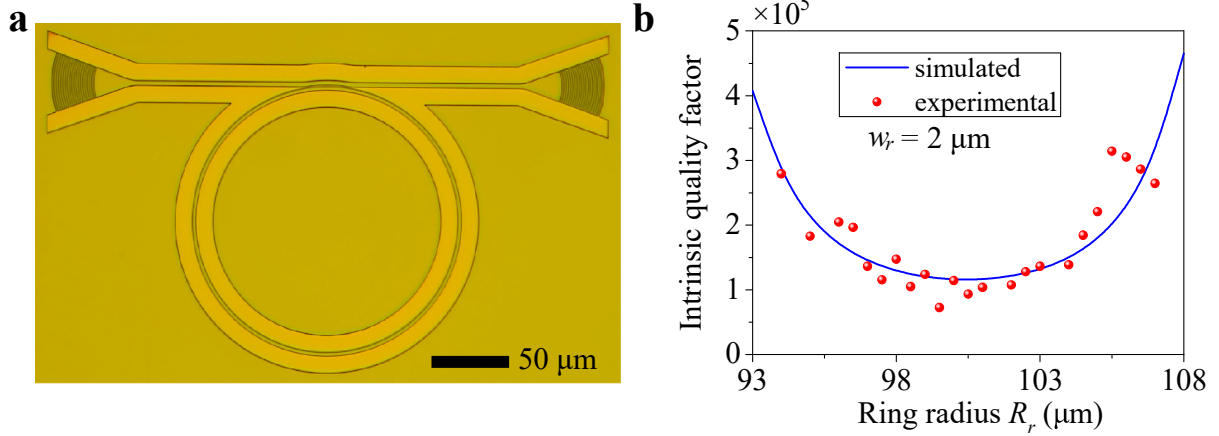


Fig. S10. (a) Optical microscope image of a microring cavity. (b) Intrinsic Q factors of microring cavities with different radii.

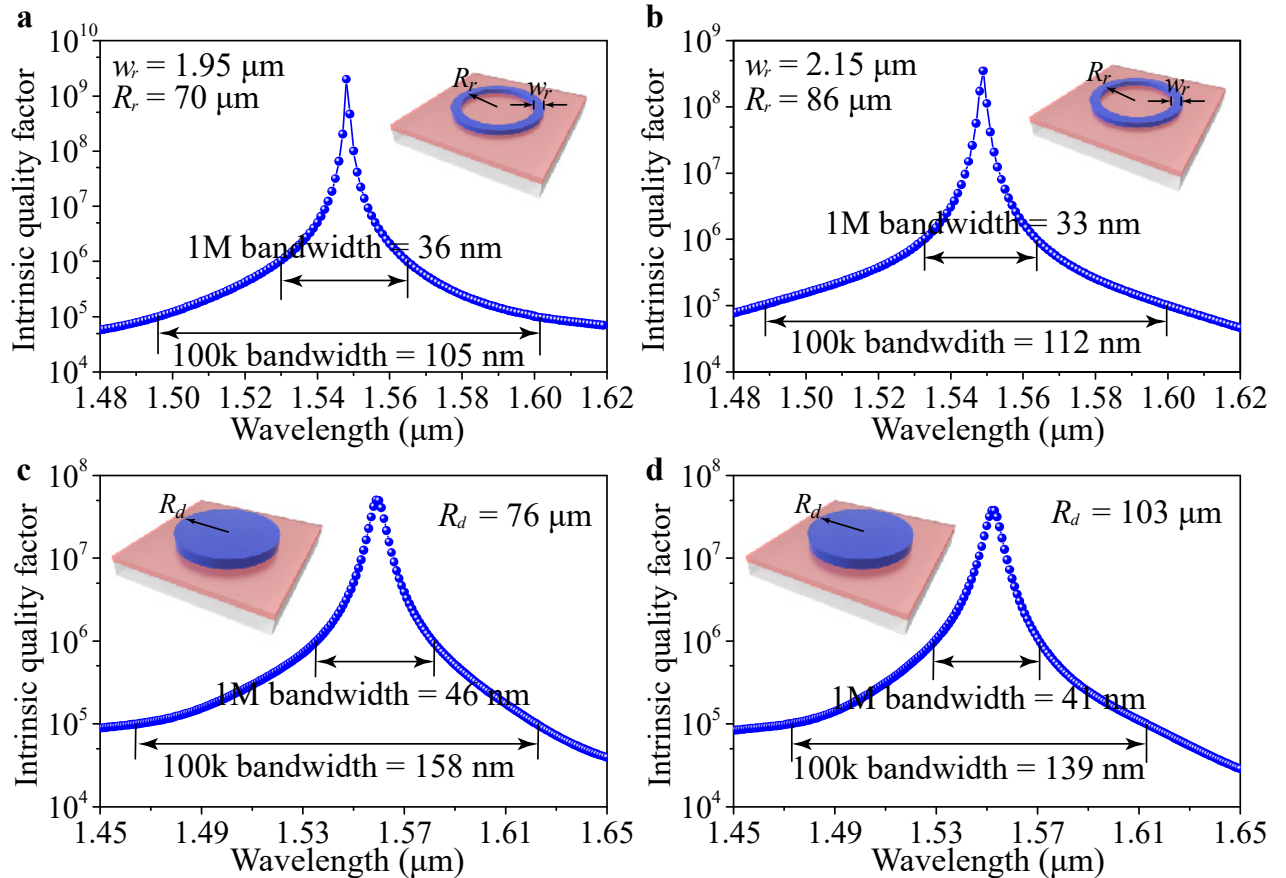


Fig. S11. (a),(b) Wavelength-dependent intrinsic quality factors of microring cavities with $(w_r, R_r) = (1.95 \mu\text{m}, 70 \mu\text{m})$ and $(2.15 \mu\text{m}, 86 \mu\text{m})$. (c),(d) Wavelength-dependent intrinsic Q factors of microdisk cavities with $R_d = 76 \mu\text{m}$ and $103 \mu\text{m}$. Both microring and microdisk cavities can possess a high Q factor in a wide band.

The Q factors of microring and microdisk cavities were analyzed at $1.55\ \mu\text{m}$ for different structural parameters. BICs with 3D confinement can be achieved for certain combinations of parameters, resulting in ultrahigh Q factors of these states. Obtaining an ultrahigh Q factor in a wide wavelength range is desired in most applications. We numerically calculated the Q factors of microring and microdisk cavities, with the parameters satisfying the BIC condition at the wavelength of $1550\ \text{nm}$. Figures S11a and S11b show the wavelength-dependent Q factors of microring cavities with $(w_r, R_r) = (1.95\ \mu\text{m}, 70\ \mu\text{m})$ and $(2.15\ \mu\text{m}, 86\ \mu\text{m})$, respectively. The Q factor for the microring with $(w_r, R_r) = (1.95\ \mu\text{m}, 70\ \mu\text{m})$ maintains above 10^6 and 10^5 in a bandwidth of $36\ \text{nm}$ and $105\ \text{nm}$, respectively. The Q factor for the microring with $(w_r, R_r) = (2.15\ \mu\text{m}, 86\ \mu\text{m})$ maintains above 10^6 and 10^5 in a bandwidth of $33\ \text{nm}$ and $112\ \text{nm}$, respectively. Figures S11c and S11d show the wavelength-dependent Q factors of microdisk cavities with $R_d = 76\ \mu\text{m}$ and $103\ \mu\text{m}$, respectively. The Q factor for the microdisk with $R_d = 76\ \mu\text{m}$ maintains above 10^6 and 10^5 in a bandwidth of $46\ \text{nm}$ and $158\ \text{nm}$, respectively. The Q factor for the microdisk with $R_d = 103\ \mu\text{m}$ maintains above 10^6 and

10^5 in a bandwidth of $41\ \text{nm}$ and $139\ \text{nm}$, respectively. The quality factors plotted in Fig. S11 neglect the absorption of the organic polymer and show that the theoretical quality factors of microring and microdisk cavities can be $>5 \times 10^7$, which is much higher than that demonstrated in the etched LiNbO_3 structures ($\sim 10^7$) [S9].

Achieving ultrahigh Q factors in a wide wavelength range has also been experimentally demonstrated in microring and microdisk cavities. Figure S12 shows SEM images of a fabricated microring cavity. The microring cavity maintains high Q factors and high extinction ratios in a wide spectral range as shown in Fig. S13a, which also confirms that bent waveguides can maintain low bending loss in a wide band. Figures S13b and S13c are the zoomed-in spectra for two individual resonances, showing the loaded and intrinsic Q factors of $\sim 5.2 \times 10^4$ and $\sim 1.5 \times 10^5$, respectively.

Figure S14 shows SEM images of a fabricated microdisk cavity. The microdisk cavity also maintains high Q factors in a wide spectral range as shown in Fig. S15a. The Lorentzian fitting of the resonances in Figs. S15b and S15c reveals the loaded and intrinsic Q factors of $\sim 4.0 \times 10^4$ and $\sim 2.3 \times 10^5$, respectively.

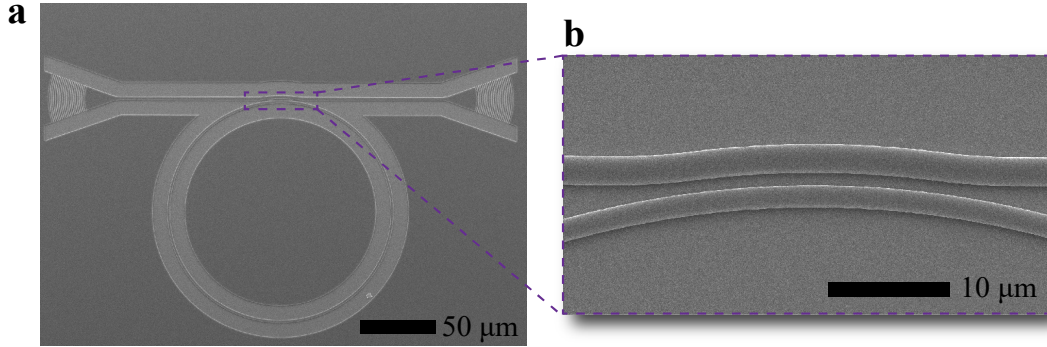


Fig. S12. (a) SEM image of a microring cavity. (b) Zoomed-in SEM image of the coupling region.

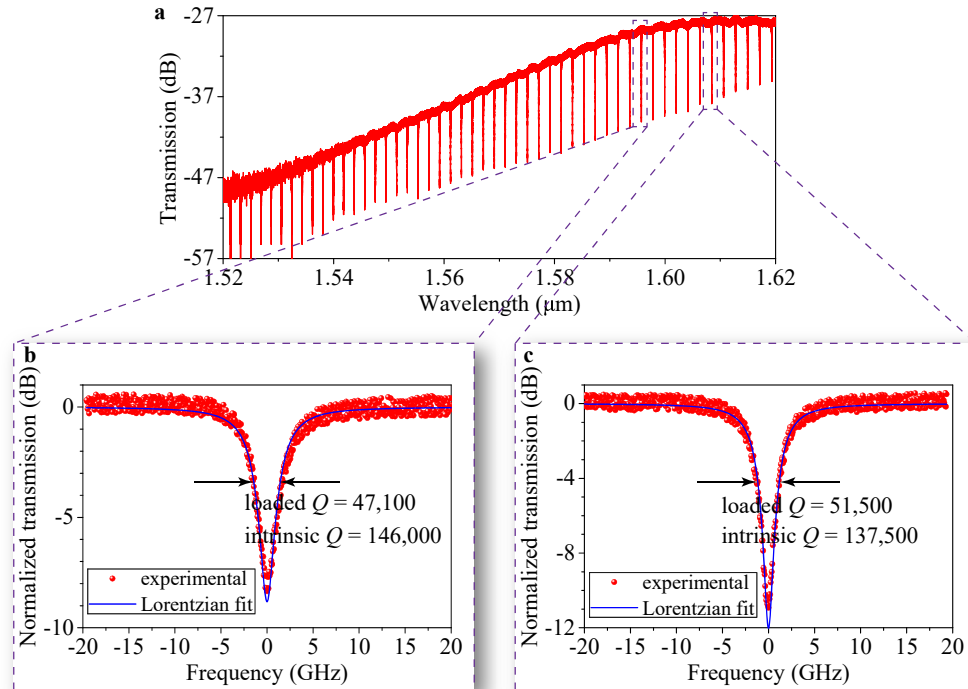


Fig. S13. (a) Measured transmission spectrum of a microring cavity, which exhibits high Q factors and high extinction ratios in a wide spectral range. (b),(c) Zoomed-in transmission spectra. The experimental results are fitted with a Lorentzian lineshape (blue lines), showing the loaded Q factors of $47,100$ and $51,500$, and intrinsic Q factors of $146,000$ and $137,500$.

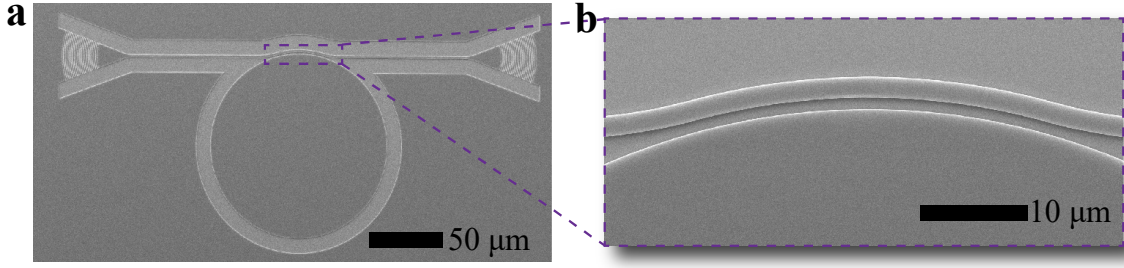


Fig. S14. (a) SEM image of a microdisk cavity. (b) Zoomed-in SEM image of the coupling region.

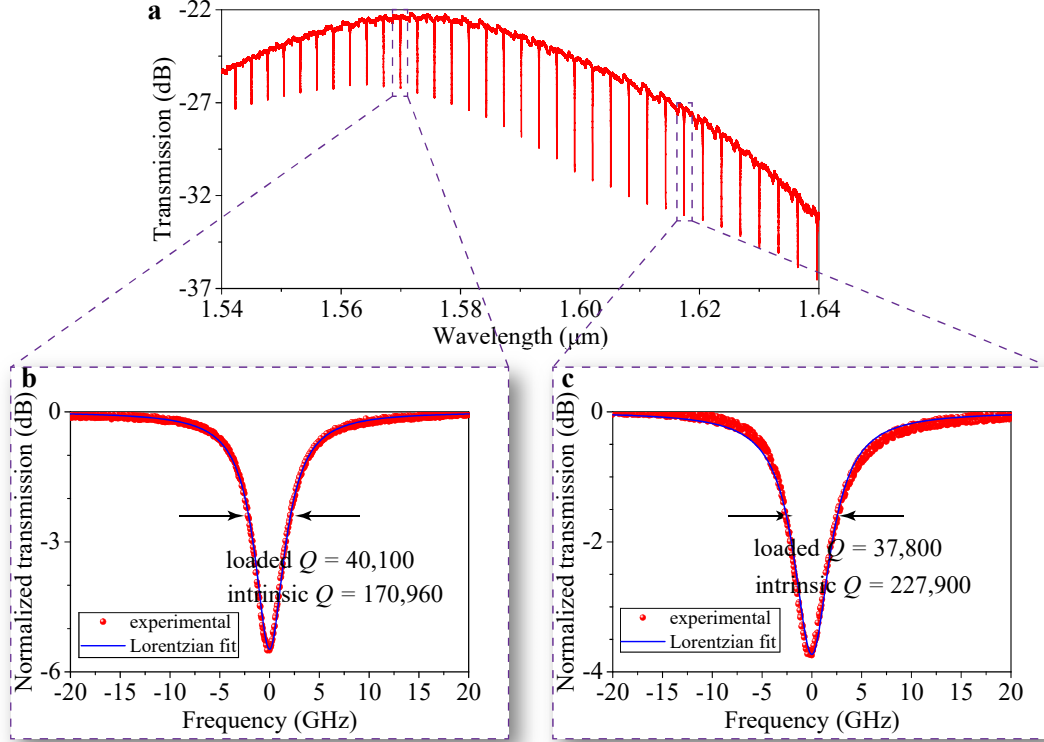


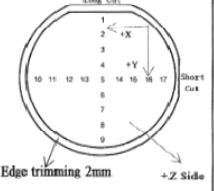
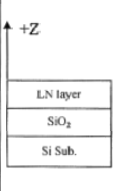
Fig. S15. (a) Measured transmission spectrum of a microdisk cavity, which exhibits high Q factors and high extinction ratios in a wide spectral range. (b),(c) Zoomed-in transmission spectra. The experimental results are fitted with a Lorentzian lineshape (blue lines), showing the loaded Q factors of 40,100 and 37,800, and intrinsic Q factors of 170,960 and 227,900.

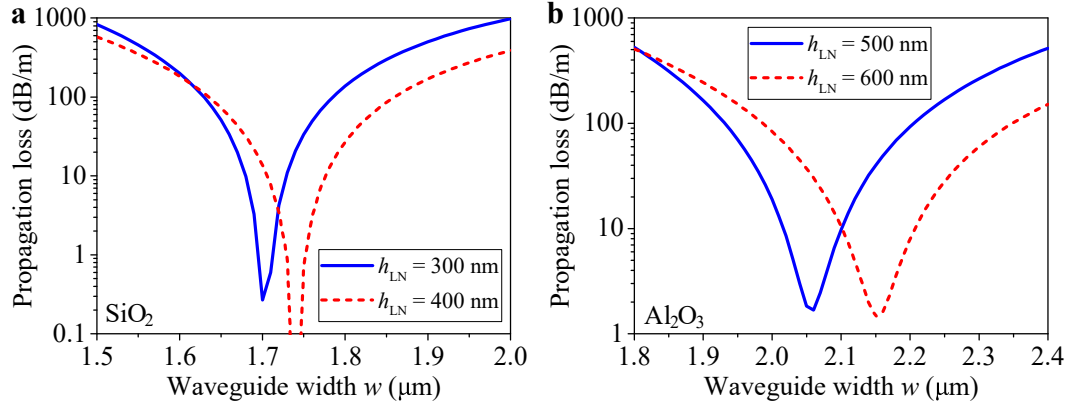
Comparing Figs. 2f and 3g in the main manuscript, we find that the BICs are achieved in microdisk cavities of different radii, where Fig. 2f shows a BIC at radius of $63\text{ }\mu\text{m}$ while Fig. 3g shows the BIC at the radius of $68.5\text{ }\mu\text{m}$. This is because of different thicknesses of the LiNbO_3 layer in the two cases, which are 300 nm in Fig. 2f and 350 nm in Fig. 3g. The LiNbO_3 wafer used in our experiment has a variation in its thickness distribution across a wafer, as shown in Table S1.

Because LiNbO_3 is transparent near $1.55\text{ }\mu\text{m}$ and has a wide bandgap to prevent two-photon absorption, the Q factor of LiNbO_3 cavities has been reported to achieve 10 million [S9]. However, the experimentally measured Q factors of our devices are limited to less than half a million. This should be attributed to light scattering at the rough sidewalls of the patterned e-beam resist and light absorption by the remaining solvent in the e-beam resist [S10]. The sidewall roughness of e-beam resist can be reduced by optimizing the e-beam lithography process

and/or performing postlithography resist reflow. Alternatively, we can adopt low-loss transparent dielectric materials like SiO_2 and atomic-layer-deposited Al_2O_3 for the low-refractive-index waveguide to improve the device performance on our proposed platform. These dielectric materials have already been utilized for demonstrating optical cavities of ultrahigh Q factors and their etching processes are already mature. For SiO_2 , on-chip optical cavities with Q factors of 2×10^8 have already been demonstrated [S11]. Taking this loss rate into consideration, Fig. S16a plots the predicted propagation loss of straight BIC waveguides with SiO_2 as the low-refractive-index material as a function of the waveguide width w . For Al_2O_3 , a reliable and reproducible deposition process for fabricating Al_2O_3 waveguides with loss as low as 0.1 dB/cm has also been developed [S12]. Taking this loss rate into consideration, Fig. S16b plots the predicted propagation loss of straight BIC waveguides with Al_2O_3 as the low-refractive-index material as a function of the waveguide width w .

Table S1. Thickness Distribution of the LiNbO₃ Wafer Used in Our Experiment

Information	Structure	Point	Top LN Thickness(nm)	SiO ₂ Thickness(nm)	Point	Top LN Thickness(nm)	SiO ₂ Thickness(nm)	Substrate Si Information
		1	370.9	2169	10	334.8	2102	thickness: 390±10 μm
		2	356.9	2086	11	326.3	2065	
		3	322.3	2070	12	308.9	2055	
		4	278.3	2031	13	281.0	2028	
		5	273.8	2007	14	283.8	2016	
		6	275.5	2005	15	310.3	2028	
		7	286.7	2013	16	328.6	2016	
		8	323.2	2022	17	315.3	2029	
		9	324.9	2033				

**Fig. S16.** Predicted propagation loss of straight BIC waveguides with SiO₂ (a) and Al₂O₃ (b) as the low-refractive-index material as a function of the waveguide width w , where h_{LN} is the thickness of the LiNbO₃ layer.

3.6. Electro-optic modulators

In addition to passive devices, we have also developed active devices by taking advantage of the unique properties of LiNbO₃ which has large electro-optic coefficients. The mechanism of electro-optic modulation is explained below.

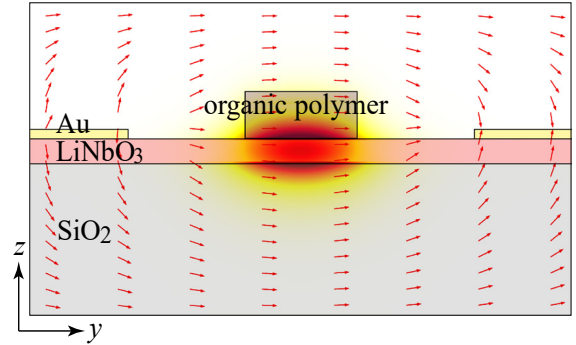
Without a voltage applied to the electrodes, the refractive index ellipsoid of LiNbO₃ is expressed as

$$\sigma_1^0 x^2 + \sigma_2^0 y^2 + \sigma_3^0 z^2 = 1, \quad (S5)$$

where $\sigma_1^0 = 1/n_o^2$, $\sigma_2^0 = 1/n_o^2$, and $\sigma_3^0 = 1/n_e^2$. When a voltage is applied to the electrodes, the generated electric field will induce a change of the refractive indices in all directions:

$$\begin{bmatrix} \sigma_1 - \sigma_1^0 \\ \sigma_2 - \sigma_2^0 \\ \sigma_3 - \sigma_3^0 \\ \sigma_4 \\ \sigma_5 \\ \sigma_6 \end{bmatrix} = \begin{bmatrix} \Delta\sigma_1 \\ \Delta\sigma_2 \\ \Delta\sigma_3 \\ \Delta\sigma_4 \\ \Delta\sigma_5 \\ \Delta\sigma_6 \end{bmatrix} = \begin{bmatrix} 0 & -\gamma_{22} & \gamma_{13} \\ 0 & \gamma_{22} & \gamma_{13} \\ 0 & 0 & \gamma_{33} \\ 0 & \gamma_{51} & 0 \\ \gamma_{51} & 0 & 0 \\ -\gamma_{22} & 0 & 0 \end{bmatrix} \begin{bmatrix} E_x \\ E_y \\ E_z \end{bmatrix}, \quad (S6)$$

where the 6×3 matrix contains the electro-optic coefficients of LiNbO₃. In our demonstrated MZI electro-optic modulators (Fig. 4e in the main manuscript), the electrodes are in parallel with the waveguide, so the electric field along the light propagation direction E_x is negligible. Figure S17 plots the numerically simulated electric field distribution across the hybrid waveguide when a voltage is applied to the electrodes. It is apparent that the electric field in the LiNbO₃ layer is mainly along the y axis, so that E_z is negligible. Therefore, the refractive index ellipsoid of a z -cut LiNbO₃ film under the applied electric field can be expressed as

**Fig. S17.** Cross-sectional distribution of electric field across the hybrid waveguide with a voltage applied to the electrodes. The BIC modal profile is superimposed on the waveguide structure.

$$(\sigma_1^0 - \gamma_{22} E_y) x^2 + (\sigma_2^0 + \gamma_{22} E_y) y^2 + \sigma_3^0 z^2 + 2\gamma_{51} E_y yz = 1. \quad (S7)$$

The effective refractive index of the propagating TM-polarized BIC mode is subject mainly to the variation of n_e . Therefore, we expect efficient electro-optic modulation for the propagating BIC mode by controlling the voltage applied to the electrodes, because the strength of E_y can be tuned to cause a variation to n_e by

$$\Delta n_e = -\frac{1}{2} n_e^3 \gamma_{51} E_y. \quad (S8)$$

The consequent variation of the effective refractive index of the TM mode can be expressed as $\eta \Delta n_e$. The phase difference between the two arms of the MZI is $4\pi \eta \Delta n_e L / \lambda$. The output power of the MZI electro-optic modulator will be

$$P \propto \cos(2\pi \eta \Delta n_e L / \lambda). \quad (S9)$$

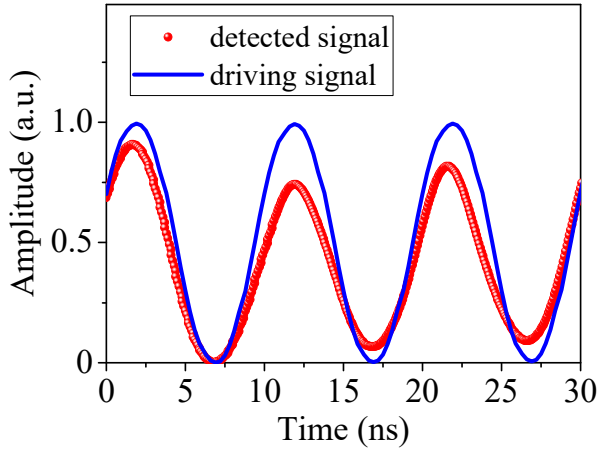


Fig. S18. Temporal response of our fabricated MZI electro-optic modulator.

Figure S18 shows the temporal response of our fabricated MZI electro-optic modulator where the blue solid line represents the sinusoidal-wave driving signal and the red dots represent the measured output optical intensity detected by a high-speed photodetector. The high fidelity between the driving and detected signals has shown that the fabricated MZI electro-optic modulator can work at a high modulation speed of at least 100 Mbps.

3.7. Second-harmonic generation

Besides its applications in electro-optic modulators, LiNbO₃ is also well known for its large second-order nonlinear optical coefficient, which is useful for research on nonlinear frequency conversion and entangled photon pair generation. Here, we analyze second-harmonic generation in a microring cavity as an example. It should be noted that degenerate parametric down-conversion is the coherent reversal process of second-harmonic generation.

The interaction between two TM bound modes at 1550 nm and 775 nm can be described by the Hamiltonian [S13]

$$H/\hbar = \omega_a a^\dagger a + \omega_b b^\dagger b + g[(a^\dagger)^2 b + a^2 b^\dagger] + \zeta_p (ae^{j\omega_p t} + a^\dagger e^{-j\omega_p t}). \quad (\text{S10})$$

Here, a (b) is the Bosonic operator for the fundamental (second-harmonic) mode in the microring with the angular frequency ω_a (ω_b), where $\omega_b = 2\omega_a$. ζ_p is the input pump field strength and ω_p is the frequency of the pump light. The nonlinear coupling strength g between the two modes can be expressed as

$$\hbar g = \epsilon_0 \iiint d\theta r dr dz \frac{3\chi^{(2)}(\mathbf{r})}{4\sqrt{2}} [u_{a,z}^*(\mathbf{r})]^2 u_{b,z}(\mathbf{r}). \quad (\text{S11})$$

Here, $\chi^{(2)}(\mathbf{r})$ is the second-order susceptibility of the nonlinear medium and ϵ_0 is the vacuum permittivity. The electric fields of optical modes in the microring cavity can be expressed as $u_{a(b),z}(\mathbf{r}) = u_{a(b),z}(\mathbf{r}, z) \exp(im_{a(b)}\theta)$ and satisfy the normalization condition

$$\hbar \omega_{a(b)}(\mathbf{r}) = \epsilon_0 \iiint d\theta r dr dz \epsilon_r(\omega_{a(b)}, \mathbf{r}) |u_{a(b),z}(\mathbf{r})|^2, \quad (\text{S12})$$

where $m_{a(b)}$ is the orbital angular momentum of mode a (b). ϵ_r is the relative permittivity of the medium as a function of frequency and position. Introducing an effective modal overlap factor at the cross section of the microring

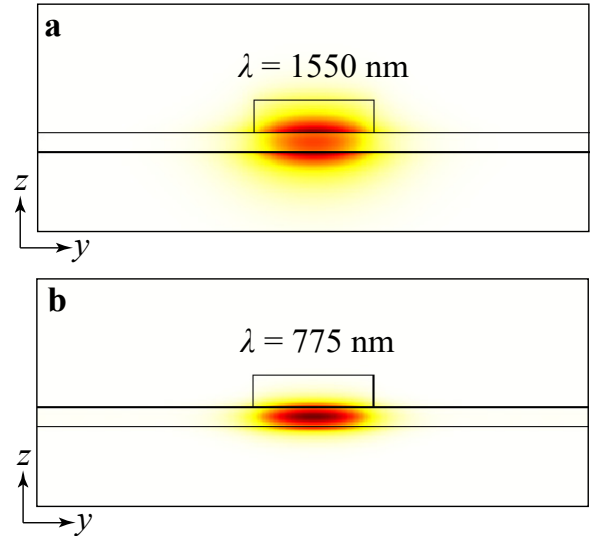


Fig. S19. (a) Electric field (E_z) profile of the fundamental mode at 1550 nm. (b) Electric field (E_z) profile of the second-harmonic mode at 775 nm.

$$\zeta = \frac{\iint dr dz [u_{a,z}^*(\mathbf{r})]^2 u_{b,z}(\mathbf{r})}{\iint dr dz |u_{a,z}(\mathbf{r})|^2 \sqrt{\iint dr dz |u_{b,z}(\mathbf{r})|^2}}, \quad (\text{S13})$$

we obtain the coupling strength

$$g \approx \zeta \sqrt{\frac{\hbar \omega_a^2 \omega_b}{\epsilon_0 2\pi R \epsilon_a \sqrt{\epsilon_b}}} \frac{1}{4\sqrt{2}} 3\chi^{(2)} \times \delta(m_b - 2m_a) \quad (\text{S14})$$

under the approximation that the microring's radius (R) is much larger than its width. Due to the azimuthal symmetry, the integral over θ yields the Kronecker delta function $\delta(m_b - 2m_a)$, so that g is nonzero only when $m_b - 2m_a = 0$, which corresponds to the momentum-conservation (phase-matching) condition.

Figures S19a and S19b show the electric field profiles of the fundamental and second-harmonic mode at the wavelength of 1550 nm and 775 nm, respectively. The second-order susceptibility of these two modes in z-cut LiNbO₃ is ~ 34.5 pm/V. The estimated single-photon nonlinear coupling strength for a microring with 50- μ m radius can achieve 2.44 MHz, which is only 1–2 orders of magnitude smaller than the intrinsic loss rate of the cavity modes. Therefore, the BIC-based PIC provides a promising platform for realizing single-photon nonlinearity for future quantum photonic applications.

4. Theoretical analysis of the photonic potential well

Figure S20 shows the cross section of the hybrid waveguide structure that is employed for demonstrating the BICs. Following the method of calculating the effective refractive index of a slab waveguide, we may divide the cross-sectional structure into three parts, where Part I and Part III are air/LiNbO₃/SiO₂ slab waveguides, and Part II is a resist/LiNbO₃/SiO₂ slab waveguide. In order to simplify the calculation, we can assume an infinite thickness for the resist layer in Part II. Because the resist possesses a higher refractive index than air, the effective refractive index of Part II is higher than those of Part I and Part III.

Light propagating in a medium of refractive index n should satisfy the wave equation

$$\nabla^2 \mathbf{E} - \mu_0 \epsilon_0 n^2 \partial_t^2 \mathbf{E} = 0, \quad (\text{S15})$$

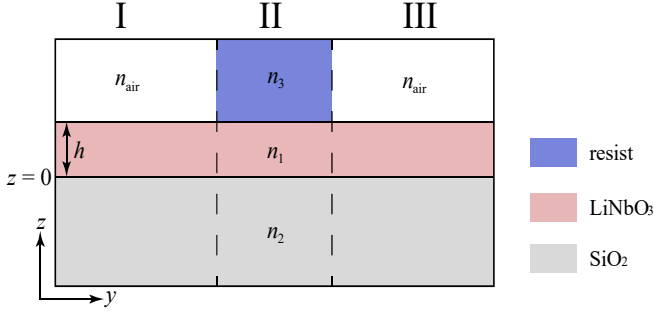


Fig. S20. Cross section of the hybrid waveguide structure that can support the BIC.

where μ_0 and ϵ_0 are the permeability and permittivity of the vacuum, respectively. First, we study the TE polarization with vanishing E_x , E_z , and H_y components, so Eq. (S15) becomes

$$\partial_x^2 E_y + \partial_z^2 E_y - \mu_0 \epsilon_0 n^2 \partial_t^2 E_y = 0. \quad (\text{S16})$$

A trial solution of Eq. (S16) is $E_y = e_y(z) \exp[j(\omega t - \beta x)]$. Substituting it into Eq. (S16), we get

$$\partial_z^2 e_y + (n^2 k_0^2 - \beta^2) e_y = 0. \quad (\text{S17})$$

For the slab waveguide in Part I and Part III, the medium consists of three layers for which Eq. (S17) should be expressed separately as

$$\begin{cases} \partial_z^2 e_y + (n_1^2 k_0^2 - \beta^2) e_y = 0 & 0 \leq z \leq h \\ \partial_z^2 e_y + (n_2^2 k_0^2 - \beta^2) e_y = 0 & z \leq 0 \\ \partial_z^2 e_y + (n_{\text{air}}^2 k_0^2 - \beta^2) e_y = 0 & z \geq h \end{cases} \quad (\text{S18})$$

In order to guide light waves in the LiNbO₃ layer ($0 \leq z \leq h$), it is necessary to have $n_1^2 k_0^2 - \beta^2 \geq 0$, $n_2^2 k_0^2 - \beta^2 \leq 0$, and $n_{\text{air}}^2 k_0^2 - \beta^2 \leq 0$. Therefore, Eq. (S18) is rewritten as

$$\begin{cases} \partial_z^2 e_y + b_1^2 e_y = 0 & 0 \leq z \leq h \\ \partial_z^2 e_y - b_2^2 e_y = 0 & z \leq 0 \\ \partial_z^2 e_y - b_{\text{air}}^2 e_y = 0 & z \geq h \end{cases} \quad (\text{S19})$$

where $b_1 = \sqrt{n_1^2 k_0^2 - \beta^2}$, $b_2 = \sqrt{\beta^2 - n_2^2 k_0^2}$, and $b_{\text{air}} = \sqrt{\beta^2 - n_{\text{air}}^2 k_0^2}$. The solutions of Eq. (S19) can be

expressed as

$$e_y(z) = \begin{cases} A \cos(b_1 z) + B \sin(b_1 z) & 0 \leq z \leq h \\ C \exp[b_2 z] & z \leq 0 \\ D \exp[-b_{\text{air}}(z - h)] & z \geq h \end{cases} \quad (\text{S20})$$

From the Maxwell equation

$$\nabla \times \mathbf{E} = -\mu_0 \partial_t \mathbf{H}, \quad (\text{S21})$$

we can get the H_x component

$$H_x = \frac{1}{j\omega\mu_0} \partial_z e_y \exp[j(\omega t - \beta x)]$$

$$= \frac{\exp[j(\omega t - \beta x)]}{j\omega\mu_0} \begin{cases} -b_1 A \sin(b_1 z) + b_1 B \cos(b_1 z) & 0 \leq z \leq h \\ b_2 C \exp(b_2 z) & z \leq 0 \\ -b_{\text{air}} D \exp[-b_{\text{air}}(z - h)] & z \geq h \end{cases} \quad (\text{S22})$$

The boundary conditions require that the tangential components of \mathbf{E} and \mathbf{H} be continuous at the interfaces $z = 0$ and $z = h$, yielding

$$\begin{cases} \partial_z^2 e_y + (n_1^2 k_0^2 - \beta^2) e_y = 0 & 0 \leq z \leq h \\ \partial_z^2 e_y + (n_2^2 k_0^2 - \beta^2) e_y = 0 & z \leq 0 \\ \partial_z^2 e_y + (n_{\text{air}}^2 k_0^2 - \beta^2) e_y = 0 & z \geq h \end{cases} \quad (\text{S23})$$

Solving Eq. (S23), we arrive at the relationship between b_1 , b_2 , b_{air} , and h as

$$\tan(b_1 h) = \frac{b_1 (b_{\text{air}} + b_2)}{b_1^2 - b_2 b_{\text{air}}}. \quad (\text{S24})$$

If we define the normalized propagation constant b , normalized frequency V , and asymmetry parameter a as

$$b = \frac{\beta^2 - n_2^2 k_0^2}{(n_1^2 - n_2^2) k_0^2} = \frac{b_2^2}{b_1^2 + b_2^2}, \quad (\text{S25})$$

$$V = k_0 h \sqrt{n_1^2 - n_2^2} = h \sqrt{b_1^2 + b_2^2}, \quad (\text{S26})$$

$$a = \frac{n_2^2 - n_{\text{air}}^2}{n_1^2 - n_2^2} = \frac{b_{\text{air}}^2 - b_2^2}{b_1^2 + b_2^2}, \quad (\text{S27})$$

we obtain the b - V equation from Eq. (S24) as

$$\tan(V \sqrt{1-b}) = \sqrt{1-b} \frac{\sqrt{b} + \sqrt{a+b}}{1-b-\sqrt{b(a+b)}}. \quad (\text{S28})$$

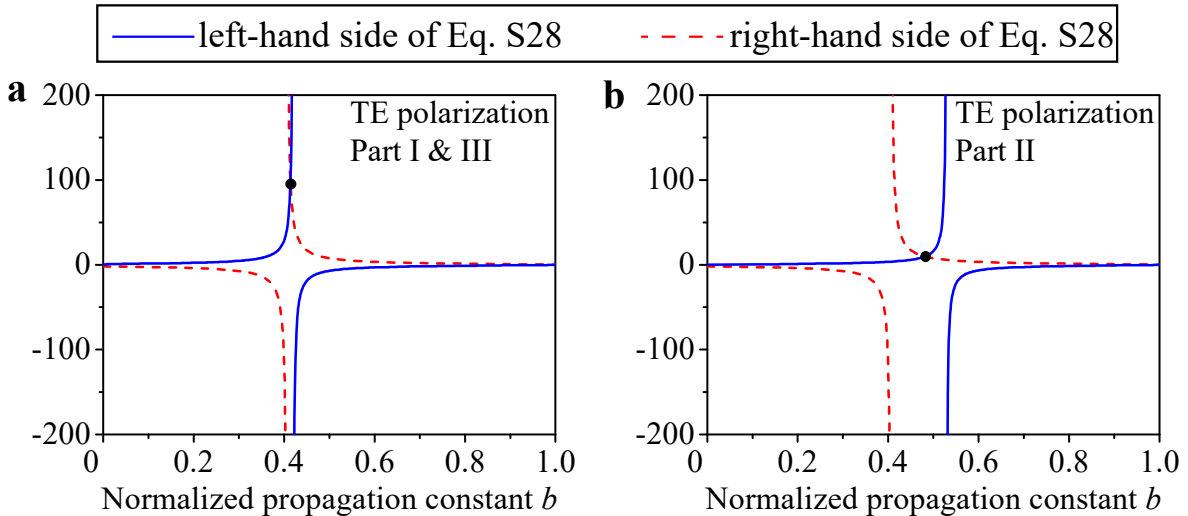


Fig. S21. Analytical calculation of the effective refractive index for the TE polarization in Part I and Part III (a) and in Part II (b) of the hybrid waveguide structure shown in Fig. S20. The blue solid and red dashed lines plot the values of the left-hand side and right-hand side of Eq. (S28), respectively. Their intersecting point provides the value of b , which is the solution to Eq. (S28).

We apply Eq. (S28) to the hybrid waveguide structure shown in Fig. S20. The thickness of the LiNbO₃ layer is 300 nm, the refractive index of SiO₂ is 1.44, and the refractive index of LiNbO₃ for the TE polarization is 2.21. Therefore, the normalized frequency for light at 1.55 μm is 2.0387, and the asymmetry parameter a is 0.3820. As shown in Fig. S21a, the intersecting point of the blue solid and red dashed lines provides the solution to Eq. (S28), $b = 0.414$, so we obtain the propagation constant in Part I and Part III, $\beta_I = 7.2934 \times 10^6$ rad/s, and the corresponding effective refractive index $n_{I(\text{TE})} = 1.7992$. With the refractive index of the resist 1.5429, the effective refractive index for the TE polarization in Part II can be calculated similarly, yielding $n_{II(\text{TE})} = 1.8508$.

Next, we study the TM polarization with vanishing H_x , H_z , and E_y components. Similar to the treatment for the TE polarization, we get $H_y = h_y(z)\exp[j(\omega t - \beta x)]$ where

$$h_y(z) = \begin{cases} A\cos(b_1 z) + B\sin(b_1 z) & 0 \leq z \leq h \\ C\exp[b_2 z] & z \leq 0 \\ D\exp[-b_{\text{air}}(z - h)] & z \geq h \end{cases} \quad (\text{S29})$$

From the Maxwell equation

$$\nabla \times \mathbf{H} = \epsilon_0 n^2 \partial_t \mathbf{E}, \quad (\text{S30})$$

we can get the E_x component

$$E_x = -\frac{1}{j\omega\epsilon_0 n^2} \partial_z h_y \exp[j(\omega t - \beta x)]$$

$$= -\frac{\exp[j(\omega t - \beta x)]}{j\omega\epsilon_0} \begin{cases} \frac{b_1 B \cos(b_1 z)}{n_1^2} - \frac{b_1 A \sin(b_1 z)}{n_1^2} & 0 \leq z \leq h \\ \frac{b_2 C}{n_2^2} \exp(b_2 z) & z \leq 0 \\ -\frac{b_{\text{air}} D}{n_{\text{air}}^2} \exp[-b_{\text{air}}(z - h)] & z \geq h \end{cases} \quad (\text{S31})$$

Applying the boundary conditions for H_y and E_x at the interfaces $z = 0$ and $z = h$, we arrive at

$$\tan(b_1 h) = \frac{b_1 \left(\frac{n_1^2}{n_{\text{air}}^2} b_{\text{air}} + \frac{n_1^2}{n_2^2} b_2 \right)}{b_1^2 - \frac{n_1^4}{n_{\text{air}}^2 n_2^2} b_2 b_{\text{air}}}. \quad (\text{S32})$$

With the normalized propagation constant b , normalized frequency V , and asymmetry parameter a defined in Eqs. (S25)–(S27), we obtain the b – V equation for the TM polarization as

$$\tan(V\sqrt{1-b}) = \frac{b}{\sqrt{1-b}} \frac{\frac{n_1^2}{n_{\text{air}}^2} \sqrt{b} + \frac{n_1^2}{n_2^2} \sqrt{b+a}}{1-b - \frac{n_1^4}{n_{\text{air}}^2 n_2^2} \sqrt{b(b+a)}}. \quad (\text{S33})$$

LiNbO₃ is an anisotropic material. Its refractive index for the TM polarization is 2.13. The normalized frequency for light at 1.55 μm is 1.9087. As shown in Fig. S22a, the intersecting point of the blue solid and red dash lines provides the solution to Eq. (S33), $b = 0.0742$, so we obtain the corresponding effective refractive index in Part I and Part III, $n_{I(\text{TM})} = 1.5021$. The effective refractive index for the TM polarization in Part II can be calculated similarly, yielding $n_{II(\text{TM})} = 1.6548$. For clarity purposes, the above theoretically calculated effective refractive index distributions are also plotted in Fig. S23 as red solid lines for both the TE and TM polarizations.

To support the analytical calculation of the effective refractive indices, we also performed FDTD simulation with commercial software Lumerical, with the results shown in Fig. S23 as blue dashed lines for both the TE and TM polarizations. In simulation, we set the thickness of the resist layer to be 500 nm which is the actual value in our fabricated devices. It is clear that the analytical and simulated results agree very well with each other.

Comparing the Schrödinger equation

$$-\frac{\hbar^2}{2m} \partial_y^2 \psi(y) + U(y)\psi(y) = E\psi(y) \quad (\text{S34})$$

with the wave equation

$$\partial_y^2 \psi(y) + n^2(y)k_0^2 \psi(y) = \beta^2 \psi(y), \quad (\text{S35})$$

it is easy to find that the potential distribution $U(y)$ for photons is inversely related to the refractive index distribution $n^2(y)$. Therefore, we can calculate the photonic potential distributions for the hybrid waveguide structure in Fig. S20 with the results shown in Fig. S24. It is clear that the TM potential well can support a TM bound mode, which lies in the spectrum of the TE continuous modes.

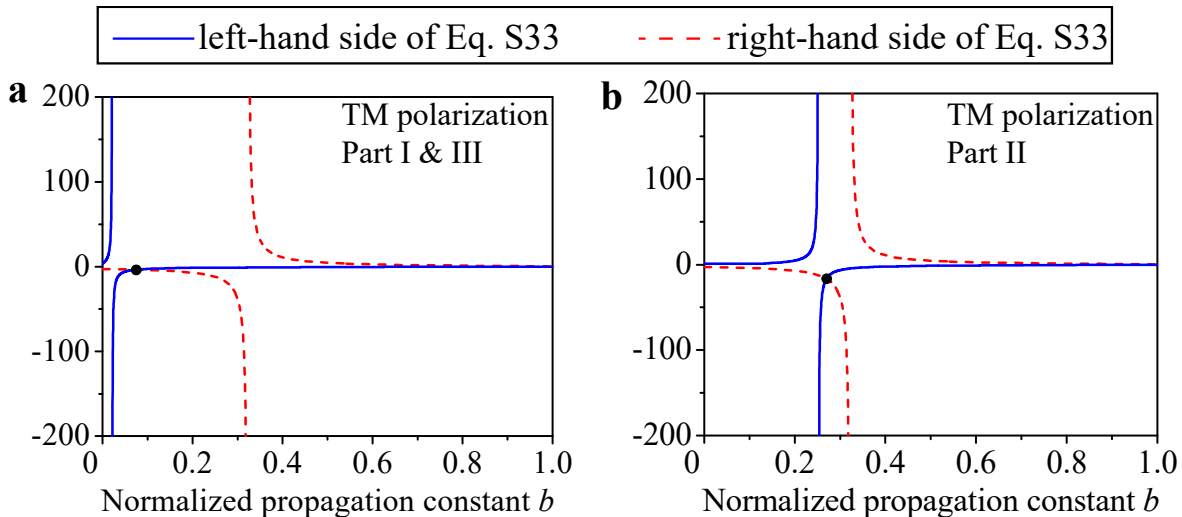


Fig. S22. Analytical calculation of the effective refractive index for the TM polarization in Part I and Part III (a) and in Part II (b) of the hybrid waveguide structure shown in Fig. S20. The blue solid and red dashed lines plot the values of the left-hand side and right-hand side of Eq. (S33), respectively. Their intersecting point provides the value of b , which is the solution to Eq. (S33).

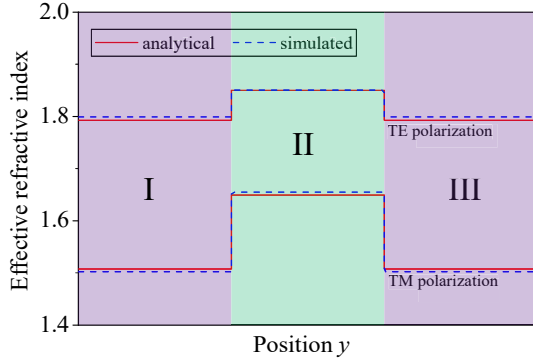


Fig. S23. Effective refractive index distribution of the hybrid waveguide structure shown in Fig. S20 for both the TE and TM polarizations.

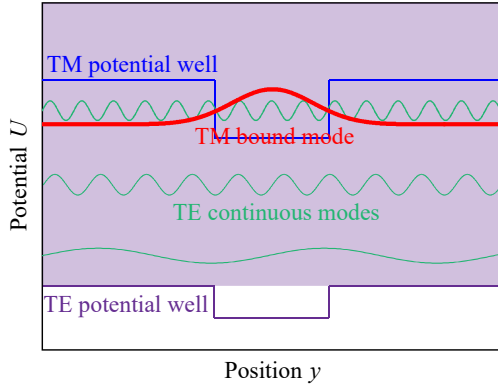


Fig. S24. Photonic potential distribution of the hybrid waveguide structure shown in Fig. S20. The purple and blue lines plot the potential wells for photons of the TE and TM polarizations, respectively. The purple region represents the TE continuous band as it is above the TE potential well. The green lines represent the TE continuous modes. The red line represents the TM bound mode which lies in the band of the TE continuous modes.

5. Theoretical analysis of the propagation loss

Given the photonic potential distributions, it is intuitively obvious that the TM bound mode can dissipate into the TE continuous modes because the TM mode's eigenenergy is located inside the continuum of the TE modes. The coupling process can be described with the following Hamiltonian [S14]

$$H/\hbar = \beta_b b^\dagger b + \sum_m \beta_m c_m^\dagger c_m + \sum_m g_m (c_m^\dagger b + c_m b^\dagger). \quad (\text{S36})$$

Here, b and c_m are the annihilation operators of the TM bound mode and the m th TE continuous mode, respectively, with β_b and β_m the corresponding propagation constants. g_m is the strength of coupling between the TM bound mode and the m th TE continuous mode.

In order to obtain an analytical expression for the coupling strength g_m , we first study a variant of the hybrid waveguide structure shown in Fig. S20, where the $\text{LiNbO}_3/\text{SiO}_2$ substrate has a finite width s in the y direction, as shown in the inset of Fig. S25a. In this variant structure, the TE continuous modes are actually discretized under the quantization condition $k_y s = 2\pi m$, and the wave vector along the y direction is $k_y = \sqrt{n_{\text{TE}}^2 - n_m^2} k_0$, where n_m is the modal index of the m th TE continuous mode ($n_m = \beta_m/k_0$) and k_0 is the wave vector in the vacuum. Figure S25a shows the numerically solved modal indices of the TE continuous modes and the TM bound mode as a function of the substrate width s . When their dispersion curves meet ($n_m \approx n_b$), we find a crossing when m is odd and an anticrossing when m is even. This is because the TM bound mode can contain some E_y component due to diffraction at the two edges of the waveguide. When m is odd, the TM bound mode is orthogonal to the m th TE continuous mode so their dispersion curves cross each other without interplay. When m is even, the nonzero overlap between the modal fields of the TM bound mode and the TE continuous mode causes their coupling so their dispersion curves exhibit an anticrossing.

Due to the modal coupling, the eigenmodes of the hybrid waveguide are actually the result of hybridization of the TM bound mode and the TE continuous modes, where the difference between the modal indices of the new eigenmodes is $\delta = \sqrt{4g_m^2 + \Delta^2}/k_0$. This means that the nonzero g_m leads to an anticrossing when $\Delta \sim 0$. As an example, Fig. S25b shows the detail of the anticrossing between the TM bound mode and the 16th TE continuous mode. When the modal indices of the two modes match ($n_{16} = n_b$), the separation between the two eigenmode branches reaches the minimum ($\delta = 2g_{16}/k_0$).

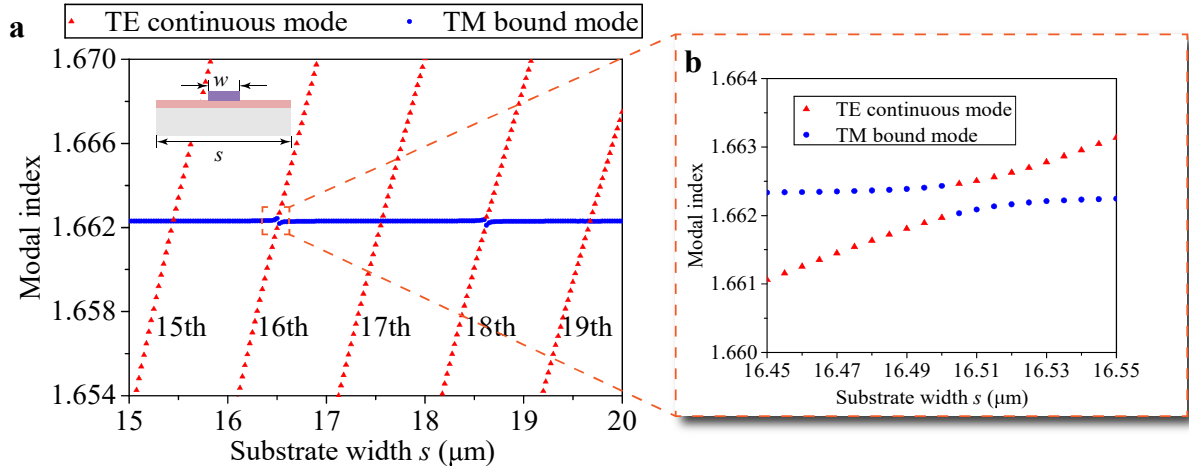


Fig. S25. (a) Modal indices of the TE continuous modes (red triangles) and TM bound mode (blue dots) as a function of the substrate width s . (b) Close-up of the anticrossing between the 16th TE continuous mode and the TM bound mode.

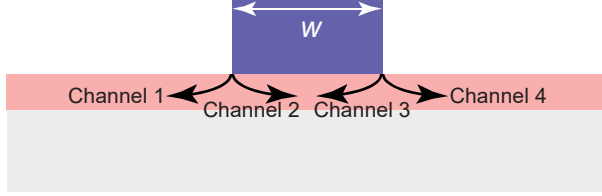


Fig. S26. Radiation channels of the TM bound mode to the TE continuum.

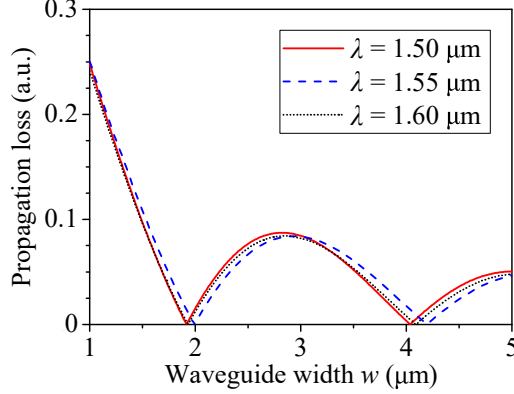


Fig. S27. Analytically calculated propagation loss of the TM bound mode supported by the hybrid waveguide structure shown in Fig. S20, as a function of the waveguide width w .

Table S2. Parameters for Obtaining the BIC with Different Methods

	Wavelength λ (μm)	Waveguide width w (μm)
Experimental (Fig. 3b)	1.55	1.95
Numerical (Fig. 3b)	1.55	1.80
Analytical (Fig. S25)	1.55	1.97

For structures with a finite substrate width s , the total coupling strength of the TM bound mode with the m th left-propagating and right-propagating TE continuous modes can be expressed as [S14]

$$g_m \approx \tilde{g}_m \frac{|1 - e^{ik_y w}|}{2w\sqrt{s}}, \quad (\text{S37})$$

where $k_y w \approx \sqrt{n_{\text{II(TE)}}^2 - n_m^2} k_0 w$ is the phase difference between the two interfering coupling channels. \tilde{g}_m is a constant that can be obtained from numerical simulation. Equation (S37) unveils the physical mechanism for eliminating the loss of a bound mode to the continuum: *constructing multiple loss channels and controlling their phase difference to realize destructive interference between them.*

For structures with an infinite substrate width ($s \rightarrow \infty$), the coupling of the TM bound mode with the TE continuous modes leads to the Markov system–environment interaction [S15]. The optical power of the TM bound mode will decay exponentially as it propagates, $I(x) = I(0)e^{-x/L}$. With the density of the TE continuous modes

$$\rho \approx \frac{n_b s}{\sqrt{n_{\text{II(TE)}}^2 - n_b^2}}, \quad (\text{S38})$$

the decay length L of the TM bound mode can be expressed as [S14]

$$L = \frac{1}{2g_m^2 \rho} \approx \frac{w^2}{\tilde{g}_m^2 \sin^2(k_y w/2)} \frac{\sqrt{n_{\text{II(TE)}}^2 - n_b^2}}{2n_b}, \quad (\text{S39})$$

where $n_b = \beta_b/k_0$ denotes the modal index of the TM bound mode. It turns out that L does not depend on the substrate width s , because the s dependence in g_m and ρ is canceled out. Therefore, the properties of the TM bound mode for structures with a finite s should also apply to those with an infinite s , and thus we can obtain L by solving g_m and ρ for structures with a finite s .

According to Eq. (S39), the decay length of the TM bound mode can reach infinity ($L \rightarrow \infty$) for certain waveguide widths. For structures that satisfy the condition $\sin(k_y w/2) = 0$, the power dissipation to the TE continuum is forbidden because of destructive interference, leading to a theoretically lossless BIC mode. This phenomenon can also be understood intuitively with a model shown in Fig. S26: The loss of the TM bound mode to the TE continuum occurs at the two waveguide edges. The loss at each edge originates from the coupling of the TM bound mode with the left-going (Channels 1 and 3) and right-going (Channels 2 and 4) TE continuous modes. If the losses via Channels 1 (2) and 3 (4) interfere destructively and cancel with each other, then the total loss of the TM bound mode to the TE continuum can be reduced to zero, leading to a lossless TM bound mode which is the desired BIC. The inference of losses via Channels 1 (2) and 3 (4) depends on the phase difference caused by the finite width of the waveguide, so the BIC can be obtained just by optimizing the waveguide width w .

To support this theory, we calculated the propagation loss based on the expression of the decay length L in Eq. (S39) with the numerically obtained coupling strength. Figure S27 plots the calculated results for three different wavelengths $\lambda = 1.50, 1.55$, and $1.60 \mu\text{m}$. They exhibit a varying trend that is very similar to the experimental and simulated results shown in Fig. 3b in the main manuscript. For comparison, Table S2 lists the parameters for obtaining a BIC mode with different methods. It is clear that the experimental, numerical, and analytical results all agree well with each other.

References

1. D. Taillaert, P. Bienstman, and R. Baets, "Compact efficient broadband grating coupler for silicon-on-insulator waveguides," *Opt. Lett.* **29**, 2749–2751 (2004).
2. X. Guo, C.-I. Zou, C. Schuck, H. Jung, R. Cheng, and H. X. Tang, "Parametric down-conversion photon-pair source on a nanophotonic chip," *Light Sci. Appl.* **6**, e16249 (2017).
3. L. Liu, Y. Ding, K. Yvind, and J. M. Hvam, "Silicon-on-insulator polarization splitting and rotating device for polarization diversity circuits," *Opt. Express* **19**, 12646–12651 (2011).
4. J. Wang, S. He, and D. Dai, "On-chip silicon 8-channel hybrid (de)multiplexer enabling simultaneous mode- and polarization-division-multiplexing," *Laser Photonics Rev.* **8**, L18–L22 (2014).
5. D. Kwong, A. Hosseini, Y. Zhang, and R. T. Chen, "1 × 12 Unequally spaced waveguide array for actively tuned optical phased array on a silicon nanomembrane," *App. Phys. Lett.* **99**, 051104 (2011).
6. S. Chen, Y. Shi, S. He, and D. Dai, "Compact monolithically-integrated hybrid (de)multiplexer based on silicon-on-insulator nanowires for PDM-WDM systems," *Opt. Express* **23**, 12840–12849 (2015).
7. T. Li, J. Zhang, H. Yi, W. Tan, Q. Long, Z. Zhou, X. Wang, and H. Wu, "Low-voltage, high speed, compact silicon modulator for BPSK modulation," *Opt. Express* **21**, 23410–23415 (2013).
8. S. Tomofuji, S. Matsuo, T. Kakitsuka, and K.-i. Kitayama, "Dynamic switching characteristics of InGaAsP/InP multimode interference

- optical waveguide switch," *Opt. Express* **17**, 23380–23388 (2009).
- S9. M. Zhang, C. Wang, R. Cheng, A. Shams-Ansari, and M. Lončar, "Monolithic ultra-high-Q lithium niobate microring resonator," *Optica* **4**, 1536–1537 (2017).
- S10. B.-B. Li, Q.-Y. Wang, Y.-F. Xiao, X.-F. Jiang, Y. Li, L. Xiao, and Q. Gong, "On chip, high-sensitivity thermal sensor based on high-Q polydimethylsiloxane-coated microresonator," *Appl. Phys. Lett.* **96**, 251109 (2010).
- S11. K. Y. Yang, D. Y. Oh, S. H. Lee, Q.-F. Yang, X. Yi, B. Shen, H. Wang, and K. Vahala, "Bridging ultrahigh-Q devices and photonic circuits," *Nat. Photonics* **12**, 297–302 (2018).
- S12. K. Worhoff, J. D. B. Bradley, F. Ay, D. Geskus, T. P. Blauwendraat, and M. Pollnau, "Reliable low-cost fabrication of low-loss $\text{Al}_2\text{O}_3:\text{Er}^{3+}$ waveguides with 5.4-dB optical gain," *IEEE J. Quantum Electron.* **45**, 454–461 (2009).
- S13. X. Guo, C.-L. Zou, and H. X. Tang, "Second-harmonic generation in aluminum nitride microrings with 2500%/W conversion efficiency," *Optica* **3**, 1126–1131 (2016).
- S14. C.-L. Zou, J.-M. Cui, F.-W. Sun, X. Xiong, X.-B. Zou, Z.-F. Han, and G.-C. Guo, "Guiding light through optical bound states in the continuum for ultrahigh-Q microresonators," *Laser Photonics Rev.* **9**, 114–119 (2015).
- S15. C.-L. Zou, X.-D. Chen, X. Xiong, F.-W. Sun, X.-B. Zou, Z.-F. Han, and G.-C. Guo, "Photonic simulation of system-environment interaction: Non-Markovian processes and dynamical decoupling," *Phys. Rev. A* **88**, 063806 (2013).